The Astronomical Journal, 163:116 (11pp), 2022 March https://doi.org/10.3847/1538-3881/ac4713

Discovery of 16 New Members of the Solar Neighborhood Using Proper Motions from CatWISE2020

Tarun Kota[1], J. Davy Kirkpatrick[2], Dan Caselden[3], Federico Marocco[2], Adam C. Schneider[4,5], Jonathan Gagné[6,7], Jacqueline K. Faherty[3], Aaron M. Meisner[8], Marc J. Kuchner[9], Sarah Casewell[10], Kanishk Kacholia[11], Tom Bickle[12,13], Paul Beaulieu[12], Guillaume Colin[12], Leslie K. Hamlet[12], Jörg Schümann[12], and Christopher Tanner[12]
The Backyard Worlds: Planet 9 Collaboration

[1] Eastview High School, 6200 140th Street West, Apple Valley, MN 55124, USA; Tkota0910@gmail.com
[2] IPAC, Mail Code 100-22, Caltech, 1200 East California Boulevard, Pasadena, CA 91125, USA
[3] Department of Astrophysics, American Museum of Natural History, Central Park West at 79th Street, New York, NY 10034, USA
[4] United States Naval Observatory, Flagstaff Station, 10391 West Naval Observatory Road, Flagstaff, AZ 86005, USA
[5] Department of Physics and Astronomy, George Mason University, MS3F3, 4400 University Drive, Fairfax, VA 22030, USA
[6] Planétarium Rio Tinto Alcan, Espace pour la Vie, 4801 avenue Pierre-de Coubertin, Montréal, Québec, Canada
[7] Institute for Research on Exoplanets, Université de Montréal, Département de Physique, C.P. 6128 Succ. Centre-ville, Montréal, QC H3C 3J7, Canada
[8] NSF's National Optical-Infrared Astronomy Research Laboratory, 950 North Cherry Avenue, Tucson, AZ 85719, USA
[9] NASA Goddard Space Flight Center, Exoplanets and Stellar Astrophysics Laboratory, Code 667, Greenbelt, MD 20771, USA
[10] School of Physics and Astronomy, University of Leicester, University Road, Leicester LE1 7RH, UK
[11] Department of Computer Science, University of Minnesota, 200 Union Street Southeast, Minneapolis, MN 55455, USA
[12] Backyard Worlds
[13] School of Physical Sciences, The Open University, Kents Hill, Milton Keynes MK7 6AA, UK
Received 2021 September 12; revised 2021 December 9; accepted 2021 December 29; published 2022 February 7

Abstract

In an effort to identify nearby and unusual cold objects in the solar neighborhood, we searched for previously unidentified moving objects using CatWISE2020 proper motion data combined with machine learning methods. We paired the motion candidates with their counterparts in 2MASS, UHS, and VHS. Then we searched for white dwarf, brown dwarf, and subdwarf outliers on the resulting color–color diagrams. This resulted in the discovery of 16 new dwarfs, including 2 nearby M dwarfs (<30 pc), a possible young L dwarf, a high-motion early-T dwarf, and 3 later-T dwarfs. This research represents a step forward in completing the census of the Sun's neighbors.

Unified Astronomy Thesaurus concepts: Brown dwarfs (185); Solar neighborhood (1509); Proper motions (1295); Two-color diagrams (1724)

1. Introduction

The Wide-Field Infrared Survey Explorer (WISE; Wright et al. 2010), with its unique full-sky sensitivity, has the potential to answer fundamental astrophysical questions. From 2009 to 2011, WISE gave astronomers unparalleled photometric data on objects across the span of the universe. Using these data, there were many WISE-based discoveries, including the first Earth Trojan Asteroid (Connors et al. 2011), the most luminous galaxy (Tsai et al. 2015), and the coldest and closest known brown dwarfs (Luhman 2013; Luhman & Esplin 2014). Due to cryogen exhaustion in late 2010, WISE was forced to change from a four-band survey (W1 (3.4 μm), W2 (4.6 μm), W3 (12 μm), W4 (22 μm)) into a two-band survey (W1 and W2). The mission was repurposed as NEOWISE (Mainzer et al. 2011). Since its launch, NEOWISE has detected over 34,000 minor planets (Mainzer et al. 2014), as the detection of near-earth objects is the new scientific driver of the mission.

Nevertheless, for astronomers who were interested in identifying motion objects outside of our solar system, the only available WISE processing that leveraged the time-series data was the AllWISE catalog (Cutri et al. 2013). However, AllWISE only uses early WISE data (13-month viewing time), which means it is only able to identify brighter, high-motion objects (Kirkpatrick et al. 2014, 2016). With a short time-baseline, our ability to detect fainter moving objects and smaller motion is limited. The key factor is that fainter objects have larger positional uncertainties, which prevents us from finding faint, smaller-motion objects.

The CatWISE Preliminary Catalog (Eisenhardt et al. 2020) is a reprocessing of WISE/NEOWISE data over a 6 yr time frame (2010–2016) to measure motions of more slowly moving objects. Since NEOWISE is only a W1 and W2 survey, CatWISE Preliminary only has these two filters. CatWISE Preliminary—the richer dataset—enabled motion detection at fainter magnitudes and smaller motions.

CatWISE2020 (Marocco et al. 2021) took this one step further by adding another two years of data to the data used for the CatWISE Preliminary Catalog, bringing the total to six times as many exposures spanning over 16 times as large a time-baseline as the AllWISE catalog. In addition, the detection list for the CatWISE2020 Catalog was generated using the unWISE Catalog (Schlafly et al. 2019) instead of the AllWISE detection software used by the CatWISE Preliminary pipeline. Because of these two factors, the CatWISE2020 Catalog has almost twice as many sources as the CatWISE Preliminary Catalog. Although this improved astrometric accuracy has led to initial discoveries (Kirkpatrick et al. 2021; Meisner et al. 2021; Rothermich et al. 2021), the CatWISE2020 data are still largely unexplored.

In this paper, we use the CatWISE2020 proper motions to search for nearby and unusual cold objects that have otherwise been overlooked. Specifically, due to their low luminosity, cooler brown dwarfs comprise the majority of gaps in our knowledge of the solar neighborhood (Kirkpatrick et al. 2019). However, M dwarfs, which are the most common objects in the solar neighborhood, can also be missing due to small motions because earlier surveys may have lacked a sufficient time-baseline to identify them.

A complete census of astronomical objects in the solar neighborhood is important to determine the low-mass cutoff for star formation (Kirkpatrick et al. 2019) and would allow researchers to conduct more precisely targeted searches for habitable exoplanets around these host objects (Zechmeister et al. 2009; Gillon et al. 2017).

In this paper, we present the discovery of 16 new objects, including 2 nearby M dwarfs, a likely young L dwarf, a high-motion early-T dwarf, and 3 additional late-T dwarfs. In Section 2 we discuss the method we used to select candidates from CatWISE2020. In Section 3 we discuss the identification methods we used to select interesting objects from our candidate list. In Section 4 we characterize our most interesting new discoveries. In Section 5 we give brief conclusions.

2. Candidate Selection

We used XGBoost (Chen & Guestrin 2016) to identify rows in CatWISE2020 that may pertain to moving objects. XGBoost is a feature-rich machine learning package centered around gradient boosting. From XGBoost, we chose to train binary classification trees that output a single floating point score with values from 0.0 to 1.0 for each CatWISE2020 row. Lower scores indicate that the row is less like those of moving objects in our training set, whereas higher scores mean the row is more like them. Typically, we would explore classifier results by sorting them with higher scores first, and stop exploring results when we encounter so many false positives that we are no longer effectively using our time. Although every classifier we trained was different and had completely different score distributions, we were usually overwhelmed by false positives well before scores of 0.5.

Being a binary classification task means that the classifiers are trained to answer a "yes" or "no" question, or, thought of in another way, predict membership of two classes. For our classifiers, these are the moving object class and the nonmoving object class. The moving object class asks whether the object to which this CatWISE2020 row pertains has significant proper motion. Significant proper motion, for our methodology, is a proper motion that a human verifier could confirm by watching an animation of WISE imagery spanning approximately 10 yr. This ends up being around 50–150 mas yr^{-1}, but is different for every human verifier and for every signal-to-noise ratio of the candidate moving object. The nonmoving object class is then the complement of the moving object class: if the CatWISE2020 row does not pertain to an object with significant proper motion, it is a member of the nonmoving object class.

To construct our dataset, we took a random sample of about 200,000 rows from CatWISE2020 and temporarily assumed that none of them pertained to moving objects. This was our nonmoving object training set. The classifier would train to output scores that are low for rows like these.

Next, we took the results of a previous candidate search that contained coordinates for candidate moving objects. These objects had previously been human reviewed, and in the opinion of the humans, they exhibited discernable proper motion in WISE animations. We cross-matched these candidate moving objects with CatWISE2020 to obtain CatWISE2020 rows for each candidate. Some candidates did not have matches, some matched incorrect rows, and some matched more than one correct row. More than one correct row can happen when CatWISE2020 fits multiple detections of the same source. We plotted the cross-match results in various views such as with color, magnitude, and cross-match angular separation to identify obvious spurious matches as those whose location is different from the locations of the majority of the dataset. We eliminated these matches from our training set. We then temporarily assumed that all of the remaining matches were correct. This left us with about 4000 rows. This was our moving object training set.

We next assigned class weights to the moving and nonmoving object training set. With an imbalanced training set, weighting is crucial. As XGBoost builds classifiers, it runs partially built classifiers against the training set and measures the difference between the classifiers' predicted output versus the desired output. This difference goes into the loss function (we used the default log loss function), which is then used to calculate loss. Without any weighting, the nonmoving set will contribute $\sim$200,000 / $\sim$4000 $\approx$ 50 times more examples to the loss function than the moving set. As a result, the classifier will be incentivized to return a low score and will not train as well. To address this, class weighting is the standard approach. We chose a balanced strategy that equalizes the total weight of all members of each class. Members of the overpopulated nonmoving set were assigned a lower weight, and the training loss was scaled down by that lower weight. Members of the underpopulated moving set were assigned a higher weight, and the training loss was scaled up.

In addition to weighting by class, we also weighted the moving set using the point-spread function (PSF) fit magnitude in W2 (w2mpro in the CatWISE2020 Catalog). We divided the moving set into 0.5 mag bins and equalized the total weight in each bin. In Marocco et al. (2019), balancing weights by w2mpro was motivated by the recognition that our moving object set contained only a few very faint examples, and we desired to improve the model performance on very faint examples. We also limited rows to w2mpro $>$14.0 mag under the assumption that bright objects had been exhausted by prior searches, and we hoped that the reduced scope would enable the model to perform better for faint objects. These processes are described in more detail in Section 3 of Marocco et al. (2019).

We then removed columns that were inappropriate for classification, such as coordinates and source identifiers. Then, we added new columns, commonly called features, calculated from catalog parameters. For example, we added the signal-to-noise ratio of the W1 versus W2 profile-fit photometry $w1snr - w2snr$; the signal-to-noise ratio of profile-fit photometry without versus with the CatWISE2020 astrometric solution such as $w1snr - w1snr\_pm$; and differences in aperture photometry in the same band, but with another aperture size such as 5.″5 versus 8.″25 $w1mag\_1 - w1mag\_2$ and 8.″25 versus 11″ $w1mag\_2 - w1mag\_3$. We exhaustively added, removed, and modified features between training countless classifiers until improvements to the classifier performance

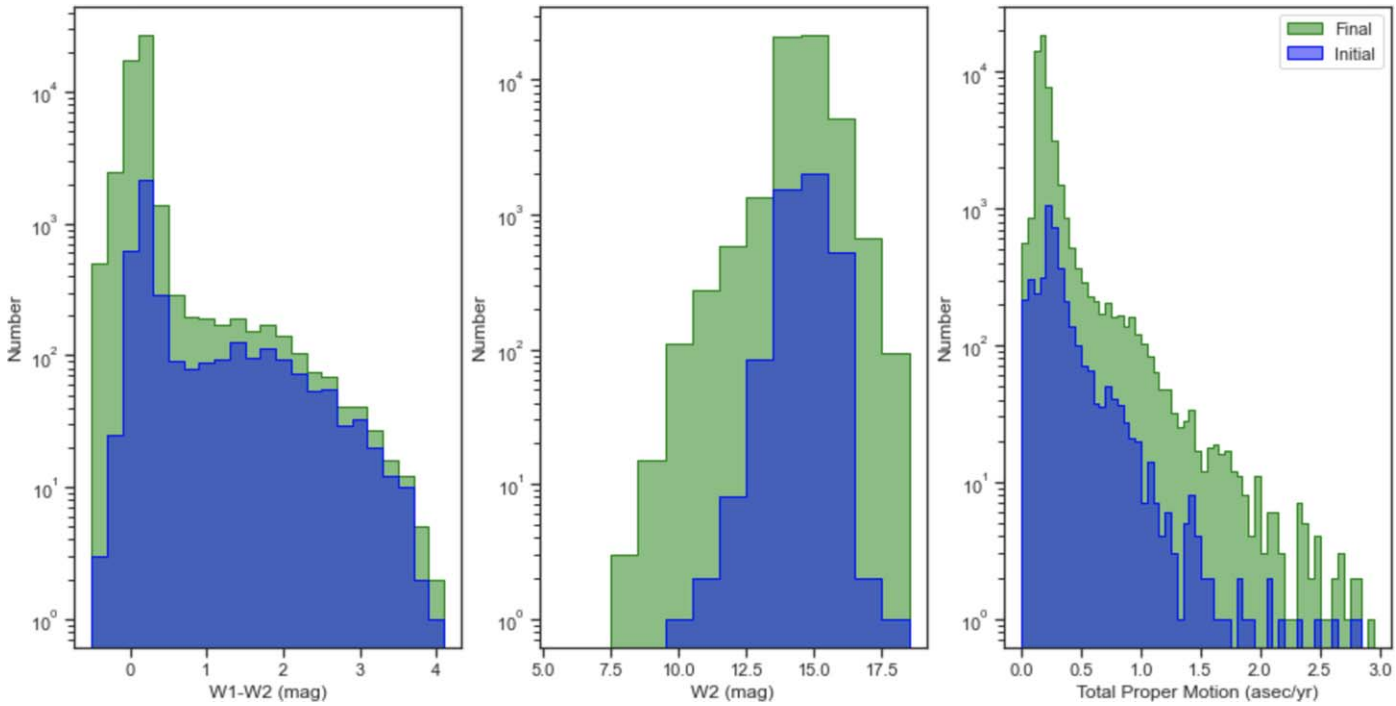

Figure 1. These histograms show the distribution of the initial (blue) and final (green) moving object training sets across W1 − W2, W2 and total proper motion. Note that for our W1 − W2 histogram we only plot objects that had W1 − W2 values between −0.5 and 4.0 mag.

were no longer statistically significant across multiple training runs. We are under no illusion that our feature set is optimal. Instead, we experimentally found that removing any individual features from the list did not improve performance and exhausted our ideas for new features.

Before training the classifier, we removed duplicate rows, randomly shuffled rows, calculated additional feature columns, and dropped nonfeature columns from the training set. Then we isolated 20% of the training set and set it aside. This would be the validation set that we would use to estimate the classifier performance during training. When the classifier performance on the validation set stopped improving, the training process would halt. Halting training early in this way is a common technique called early stopping. Because each training iteration in XGBoost adds complexity to the classifier, early stopping prevents classifiers from becoming unnecessarily complex.

Then we ran the trained classifier over all CatWISE2020 rows having w2mpro >14.0 mag. This involves, for each row, calculating additional feature columns, dropping nonfeature columns, and passing it to the classifiers prediction function which returns the score. We performed this operation on all CatWISE2020 rows within one unWISE tile footprint, or about 1/17,000 of the sky, per invocation to realize performance gains. For each row with a classifier score over 0.5, we added the score to the original CatWISE2020 row and saved the row to disk.

We then sorted the resulting rows by score, with the highest score first, and examined animations of WISE images at the coordinates for each row. We used WiseView (Caselden et al. 2018), which is an interactive online image blinking tool designed explicitly for human verification of motion candidates in WISE imagery. When the row pertained to a moving object, we would record the row as a true positive. When unsure, we recorded the row as unknown. After examining candidates sorted simply by score, we used various strategies, such as restricting rows by W1 − W2 color, proper motion, W2 magnitude, position in the sky, or a combination of these constraints.

Eventually, our sorting returned so few true positives per false positive that we stopped reviewing results. We then added all of the true positives to the moving object class of the training set, removed rows that we had marked as unknown from the training set entirely, and added all remaining rows to the nonmoving object class of the training set. Adding true positives to the moving objects class gave future classifiers more examples, thus making the classifiers more accurate. By adding false positives to the nonmoving object class, we add examples that are manually vetted and represent particularly hard examples that challenged our classifier. Both properties mean that these examples are valuable additions to the otherwise randomly sampled nonmoving class.

We repeated this process many times: training a classifier, vetting the results, and expanding the training set. Periodically, we purified our training set by running a classifier over the training set itself and re-inspecting highly scored members of the nonmoving class and lowly scored members of the moving class. Doing so identified erroneous entries that arrived in our training set through the initial random sample that created the nonmoving class, the cross-match that created the moving class, and human process errors such as copy-pasting coordinates into the wrong list.

After some iterations, new classifiers began scoring proper motion stars higher than their predecessors. Our initial moving object training set consisted more of fainter and higher proper motion objects, such as brown and white dwarfs, than lower-motion main-sequence stars. As we added more moving objects to our training set, they inevitably included more objects outside of the brown dwarf and white dwarf set. The classifiers we trained on the updated training set then became more sensitive to proper motion stars of all types. This created a feedback loop, the effects of which are apparent in Figure 1.

This figure shows distributions of the initial and final moving object training sets. The initial training set is redder in W1 − W2 colors than the final training set. This is an effect of updating the training set for each successive classifier and accepting main-sequence stars.

Proper motion main-sequence stars, despite overwhelming the human verifier, are not true contaminants in our search. Because they are so well recovered by Gaia and are so plentiful, careful accounting was not warranted. To save time for the human verifier, we cross-matched all CatWISE2020 rows that scored higher than 0.5 against a subset of Gaia DR1 with total proper motion >100 mas yr^{-1} and a separation of <6″. The proper motion and angular separation constraints were added to reduce false matches. Over results from one classifier, this process automatically labeled approximately 15,000 rows. After incorporating these automatic labels into our training set and training another classifier, this process automatically labeled approximately 24,000 rows. On the third repetition, we changed our cross-match criteria to require total proper motion >150 mas yr^{-1} and separation <5″. The third repetition resulted in about 13,000 automatic labels. These automatic labels, like all manual labels, were subjected to our periodic purification processes that aimed to eliminate bad matches.

In early iterations, each new classifier raised many previously unseen moving objects. With each iteration, however, the number of new moving objects decreased. We continued iterating until, ultimately, there were too many false positives per true positive to continue. Once the yield of new sources slowed significantly, we halted the training of other classifiers with this methodology and stopped verifying results from our existing classifiers. Of the motion candidates selected by our classifiers, we eliminated those for which there existed a Gaia DR1 astrometric solution. This left us with ∼6000 candidates, both known and unknown, for further analysis.

3. Analyzing Candidates

3.1. Other Databases

As stated earlier, CatWISE2020 only contains two magnitudes (W1 and W2). This meant that we only had access to one color (W1 − W2) when analyzing our candidates. With only one color, it is difficult to characterize objects. Thus, in order to obtain more colors, we gathered additional infrared data from Two Micron All-Sky Survey (2MASS; Skrutskie et al. 2006), from the UK Infra-Red Telescope (UKIRT) Hemisphere Survey (UHS; Dye et al. 2018), and from the Visible and Infrared Survey Telescope for Astronomy Hemisphere Survey (VHS; McMahon et al. 2013).

Using the CatWISE2020 proper motion values, we propagated the position of each source in time to predict the position at the epoch of the database we were querying. Using a cone search of 5″ around the predicted position, we collected the J (1.25 μm), H (1.65 μm), and Ks (2.2 μm) magnitudes. (UHS only has *J*-band coverage.) We used multiple databases to maximize our chances of finding ancillary data, as not all datasets cover the entire sky or probe deeply enough to detect our objects.

After we matched our candidate list with the various infrared databases, we searched for mismatched candidates. Due to the difference in epochs and uncertainty in the proper motion measurements, our predicted location was not always accurate. 2MASS, with its large epoch difference from CatWISE2020 (15–18 yr), gave us the most spurious matches. We used WiseView to verify or refute matches.

3.2. Color–Color Diagrams

The reference color–color diagrams we used are Figures 7 and 8 in Kirkpatrick et al. (2016), which plot J − W2 versus J − Ks and W1 − W2 versus J − W2, respectively. These plots contain all identified proper motion objects in the AllWISE1 (Kirkpatrick et al. 2014) and AllWISE2 (Kirkpatrick et al. 2016) motion surveys with magnitudes fainter than the nominal WISE W1 saturation limit of 8.1 mag. F, G, K, and M stars compose the dense locus, while L and T dwarfs lie on the outer sections. For a complete description, wer refer to Kirkpatrick et al. (2016).

Using TopCAT (Taylor 2005), we made a plot of our CatWISE2020 candidates with the same colors as the reference diagrams from Kirkpatrick et al. (2016). We compared our CatWISE2020 color–color plots side by side with the reference diagrams. As described further in Section 4, we then extracted candidates that fell outside the loci of the F, G, K, or M stars determined in Figures 7 and 8 of Kirkpatrick et al. (2016) and input them into a sublist. These are objects that have the highest probability of being cool brown dwarfs or other rare objects.

Next, to check the novelty of the objects recovered, we cross-checked our entire sublist with SIMBAD (Wenger et al. 2000) and other more recent or unpublished datasets (20 parsec census list from Kirkpatrick et al. 2021; Backyard Worlds candidate list; Kuchner et al. 2017; etc.) that have not yet been ingested into SIMBAD. Any previously discovered objects were removed from our sublist.

Finally, we created finder charts of the new discoveries using a publicly available PYTHON program.[14] These charts show the WISE images in all four bands and their counterparts (when there was coverage) in the three bands of 2MASS, in three bands of VHS, in three bands of the Digitized Sky Survey (DSS), in one band of UHS, in five bands of the Pan-Starrs (Chambers et al. 2016) survey, and in five bands of the Dark Energy Survey (DES; Abbott et al. 2018). First, we used the charts to further verify or refute matches. Second, we used the charts to ensure that our candidates had photometric properties across a wider wavelength range that were consistent with the classifications derived from their J − W2, J-Ks, and W1 − W2 colors.

Note that we only looked for interesting objects that had ancillary data at *J*, *H*, or *K*-s bands. Any object lacking UHS, VHS, or 2MASS data, or lacking a detection despite imaging in those datasets, will be part of a future study.

4. Interesting Objects

Our entire search yielded 16 new objects. All of the new discoveries are plotted on two color–color diagrams—J − W2 versus J − Ks (Figure 2) and W1 − W2 versus J − W2 (Figure 3). Outlying objects identified on these plots are discussed further below. The coordinates and photometry of our 16 discoveries are given in Table 1. Additionally, when available, Gaia photometry and parallaxes of our 16 discoveries are given in Table 2.

[14] Access Link: Finder Charts.

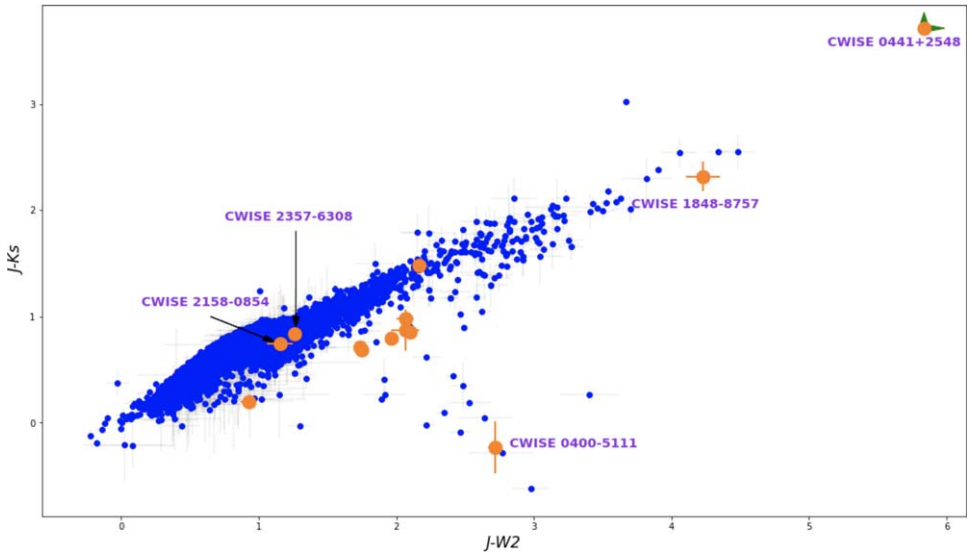

Figure 2. J − W2 vs. J-Ks color–color diagram. The orange points are discoveries announced in this paper. For comparison, other proper motion discoveries from Figure 7 of Kirkpatrick et al. (2016) are plotted as blue points. The green arrows denote color limits. Objects labeled in purple are discussed in the text. Note that the UHS discoveries are not plotted on this diagram because they have no Ks data.

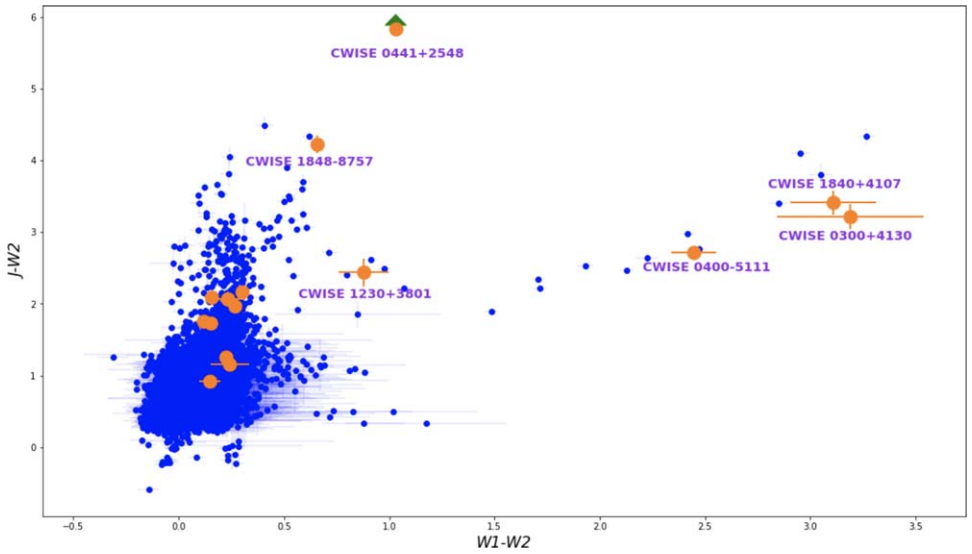

Figure 3. W1 − W2 vs. J − W2 color–color diagram. The orange points are discoveries announced in this paper. For comparison, other proper motion discoveries from Figure 8 of Kirkpatrick et al. (2016) are plotted as blue points. The green arrows denote color limits. Objects labeled in purple are discussed in the text.

4.1. CWISE J215859.63-085441.9 and CWISE J235713.17-630827.3

CWISE J215859.63-085441.9 and CWISE J235713.17-630827.3 are two nearby M dwarfs that are missing from our census of the solar neighborhood. After comparing the J − W2 colors of our objects to the data in Table 5 of Pecaut & Mamajek (2013),[15] we find that their colors most closely match those of M4 and M5 dwarfs, respectively.

Both objects were detected by Gaia EDR3 (Gaia Collaboration et al. 2016) but had no reported parallaxes. This may suggest that these objects are a part of multiple systems, confounding the short time-baseline astrometry currently available to Gaia EDR3.

We collected Transiting Exoplanet Survey Satellite (TESS; Ricker et al. 2015) time-series photometry on CWISE J235713.17−630827.3 to explore this hypothesis. We note that the location of CWISE J215859.63−085441.9 is currently not observed by TESS (at the time of this writing, September 2021). The CWISE J235713.17−630827.3 light curve is shown in Figure 4. The full light curve is shown in the top panel, and the Lomb-Scargle periodogram is shown in the bottom panel. The leftmost column is the Sector 1 30-minute light curve. The middle column shows the same plots, but for the Sector 1 2-minute light curve. Finally, the rightmost column follows the same convention as the other two, but for the Sector 28 10-minute light curve.

There are two high-powered peaks in each periodogram with periods of $P1 = 0.3028$ $+/-0.0004$ day and $P2 = 0.2646$ $+/-0.0003$ day. The implied periods are consistent over the two-year baseline. The cause for the variation is likely to be star spots rotating into and out of view. There are two possible

[15] See also: http://www.pas.rochester.edu/~emamajek/EEM_dwarf_UBVIJHK_colors_Teff.txt.

Table 1
Data for New Discoveries

CatWISE Designation (1)	J2000 R.A. (deg) (2)	J2000 Decl. (deg) (3)	μ_α (arcsec yr^{-1}) (4)	μ_δ (arcsec yr^{-1}) (5)	W1[a] (mag) (6)	W2[a] (mag) (7)	*J* (mag) (8)	*H* (mag) (9)	*K* (mag) (10)	*JHK* References (11)	Classification (12)	BYW Codiscovers[c] (13)
CWISE J015330.24-520046.6	28.3760178	−52.0129465	0.12459 ± 0.0075	0.04784 ± 0.0065	14.202 ± 0.013	14.050 ± 0.013	15.783 ± 0.005	⋯	15.076 ± 0.009	VHS	[b]	
CWISE J030009.79+413051.2	45.0408097	41.5142428	−0.26243 ± 0.0857	0.04321 ± 0.0838	19.173 ± 0.343	15.984 ± 0.065	19.199 ± 0.165	⋯	⋯	UHS[d]	T dwarf	
CWISE J040052.80-511142.5	60.2200208	−51.1951632	0.03525 ± 0.0435	−0.06973 ± 0.0443	18.274 ± .098	15.828 ± 0.037	18.547 ± 0.036	18.863 ± 0.232	18.778 ± 0.243	VHS	T dwarf	B
CWISE J044109.35+254854.4	70.2889956	25.8151209	0.14188 ± 0.0053	−0.08250 ± 0.0053	13.181 ± 0.013	12.150 ± 0.010	>17.987	16.324 ± 0.022	14.274 ± 0.074	2MASS	reddened star	
CWISE J052703.28-113056.7	81.7636813	−11.5157684	0.01655 ± 0.0185	−0.23600 ± 0.0188	14.687 ± 0.027	14.569 ± 0.027	16.320 ± 0.011	⋯	15.636 ± 0.024	VHS	[b]	
CWISE J103716.55-750257.7	159.3189815	−75.0493751	−0.19359 ± 0.0115	0.02816 ± 0.0119	15.118 ± 0.063	14.884 ± 0.056	16.948 ± 0.020	⋯	15.967 ± 0.041	VHS	L dwarf	
CWISE J120657.58-311221.1	181.7399330	−31.2058758	−0.40234 ± 0.0204	0.40390 ± 0.0233	15.766 ± 0.022	15.616 ± 0.046	16.542 ± 0.027	⋯	16.343 ± 0.055	VHS	M subdwarf	
CWISE J123041.80+380140.9	187.6741736	38.0280398	0.14901 ± 0.0743	−0.74981 ± 0.0880	17.559 ± 0.069	16.680 ± 0.095	19.117 ± 0.163	⋯	⋯	UHS	high proper motion T2 dwarf	
CWISE J125924.86−552531.8	194.8535993	−55.4255028	−0.21910 ± 0.0126	0.00887 ± 0.0144	15.126 ± 0.017	14.826 ± 0.023	16.992 ± 0.022	⋯	15.515 ± 0.022	VHS	L dwarf	
CWISE J141545.74-330545.0	213.9405948	−33.0958410	−0.17852 ± 0.0115	−0.21219 ± 0.0133	14.941 ± 0.017	14.672 ± 0.025	16.634 ± 0.018	⋯	15.839 ± 0.032	VHS	L subdwarf or early-T dwarf, A	
CWISE J144053.88-121712.3	220.2245053	−12.2867517	−0.09991 ± 0.0136	−0.23436 ± 0.0157	15.063 ± 0.019	14.906 ± 0.030	17.004 ± 0.0165	16.443 ± 0.029	16.146 ± 0.036	VHS	[b]	
CWISE J184048.17+410727.4	280.2007202	41.1242809	−0.00784 ± 0.0438	−0.06299 ± 0.0479	18.938 ± 0.199	15.829 ± 0.036	19.243 ± 0.164	⋯	⋯	UHS	T dwarf	
CWISE J184842.02-875747.9	282.1750944	−87.9633209	−0.01739 ± 0.0106	−0.15779 ± 0.0107	15.124 ± 0.019	14.465 ± 0.017	18.699 ± 0.124	⋯	16.382 ± 0.059	VHS	young L dwarf?	A,C
CWISE J210159.84-783846.8	315.4993413	−78.6463487	0.27545 ± 0.0317	−0.18208 ± 0.0301	16.489 ± 0.031	16.254 ± 0.063	18.324 ± 0.079	⋯	17.451 ± 0.176	VHS	L subdwarf or early-T dwarf	
CWISE J215859.63−085441.9	329.7484963	−8.9116413	0.0748 ± 0.0044	−0.11231 ± 0.0040	10.303 ± 0.013	10.060 ± 0.089	11.215 ± 0.026	10.708 ± 0.023	10.470 ± 0.025	2MASS	nearby M dwarf	
CWISE J235713.17−630827.3	359.3048900	−63.1409326	−0.03229 ± 0.0038	0.04222 ± 0.0034	9.798 ± 0.012	9.573 ± 0.007	10.813 ± 0.023	10.272 ± 0.022	9.997 ± 0.023	2MASS	nearby M dwarf	

Notes.
[a] These are the W1 and W2 magnitudes measured while taking into account proper motion from the CatWISE2020 Catalog (listed as w1mpro_pm and w2mpro_pm).
[b] Cannot be classified. See Section 4.4.
[c] Reference code for discoverers: *A* = Caselden, *B* = Bickle, and *C* = Goodman. These discoverers independently discovered objects in this paper using tools provided and developed for the Backyard Worlds citizen science project.
[d] Note that UHS is the only UKIRT survey our targets fell into.

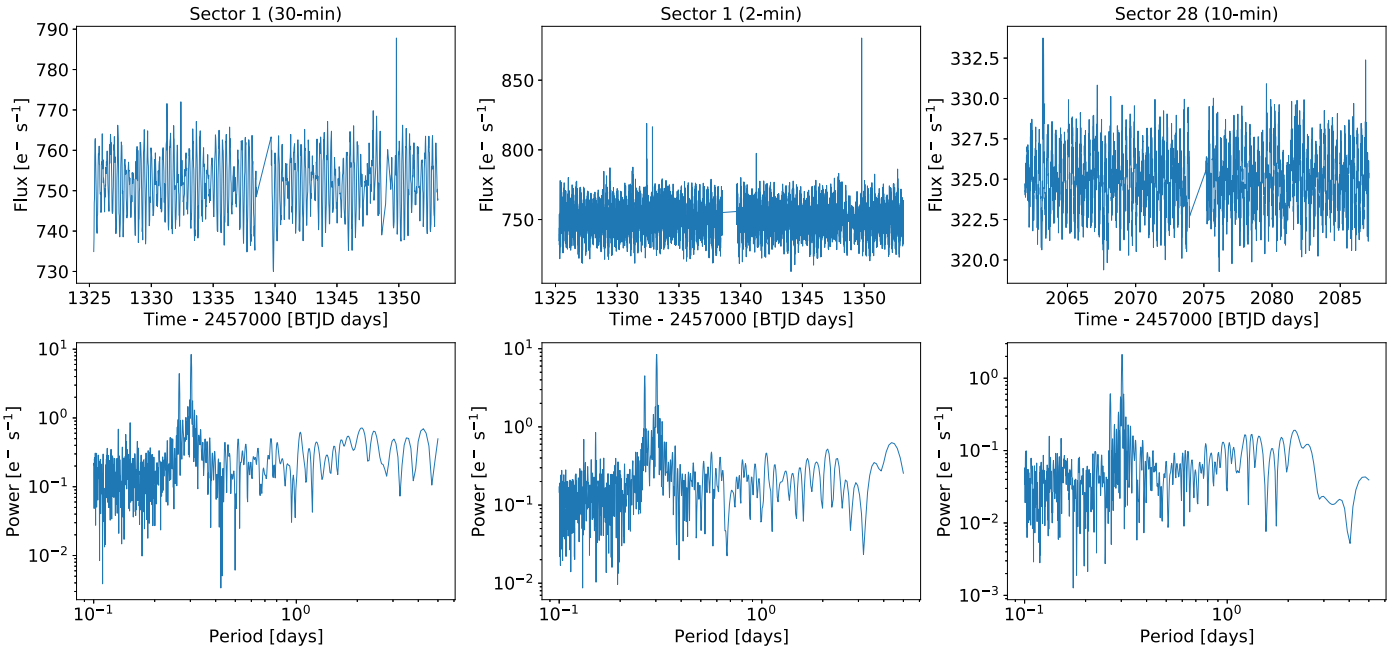

Figure 4. Time-series photometry of CWISE J235713.17−630827.3. The first row illustrates the entire light curve in three different sectors. The second row illustrates the periodogram for each of the light curves above.

Table 2
Gaia EDR3 Data on New Discoveries

CatWISE Designation	Gaia R.A. (deg)	Gaia Decl. (deg)	G (mag)	G_{BP} (mag)	G_{RP} (mag)	Plx (mas)
(1)	(2)	(3)	(4)	(5)	(6)	(7)
CWISE J015330.24-520046.6	28.375773	−52.012694	19.037842 ± 0.003477	20.801437 ± 0.166603	17.803684 ± 0.014892	4.7697 ± 0.1993
CWISE J052703.28-113056.7	81.763843	−11.516011	19.325026 ± 0.003703	20.786207 ± 0.072447	18.060532 ± 0.015927	3.2509 ± 0.2729
CWISE J120657.58-311221.1	181.739803	−31.205797	19.547705 ± 0.003853	20.997263 ± 0.114532	18.291862 ± 0.020912	6.4006 ± 0.3416
CWISE J215859.63−085441.9	329.748553	−8.911683	14.468976 ± 0.015447	15.793684 ± 0.003651	12.920640 ± 0.003923	⋯
CWISE J235713.17 −630827.3[a]	359.304944	−63.140875	14.482848 ± 0.020162	16.019608 ± 0.006164	12.760140 ± 0.004215	⋯
CWISE J235713.17 −630827.3[a]	359.304881	−63.140937	14.717904 ± 0.004546	16.005678 ± 0.007803	12.754520 ± 0.004263	⋯

Note.
[a] This CatWISE2020 object is split into two components in Gaia EDR3.

explanations for the double period. First, the object may be experiencing differential rotation like our Sun, leading to two distinct detected periods. Another explanation is that the object is a system comprised of two stars with two slightly different rotation periods. Above we surmised that Gaia reported no parallax because the object may be a multiple system. The second explanation above for the TESS double period provides some credence to this statement. The objects seen by TESS are likely to be similar in magnitude because both variations are detected in a single light curve.

Because no Gaia parallax is available, we estimate the distance as follows. With a $J-W2$ versus M_J relation for M dwarfs constructed using data from Pecaut & Mamajek (2013), we estimate the distance of CWISE J235713.17-630827.3 if it is an equal-magnitude double to be 27.5 parsecs. (If it were single, the distance estimate would be ∼23 pc). In addition, we found two sources in Gaia EDR3 that may correspond to the two components of our proposed physical pair. The separation between the sources is 0.″24. Using the G_{BP}–G_{RP} versus M_G relation found in Table 4 of Kiman et al. (2019), we estimate a M_G value of 11.86 mag and spectral type of M5 for the two Gaia sources. Then, by using the apparent G magnitude, we estimate distances of ∼33 and ∼37 pc for the two components of the binary.

Because CWISE J215859.63-085441.9 lacks a Gaia parallax, we theorize that it is also a binary like CWISE J235713.17-630827.3. Again, assuming an equal-magnitude pair and using the J–W2 versus M_J relation for M dwarfs constructed using data from Pecaut & Mamajek (2013), the distance estimate for CWISE J215859.63-085441.9 is ∼20.5 pc. (If it were single, the distance estimate would be 14.5 pc.) We found only one source in Gaia EDR3. Using the G_{BP}–G_{RP} versus M_G relation found in Table 4 of Kiman et al. (2019), we estimate an M_G value of 12.92 mag and a spectral type of M6. Then, by using the apparent G magnitude, we estimate a distance of ∼29 pc.

Despite their proximity to the Sun, these two M dwarfs were not discovered until now due to their small proper motions of $\mu_{tot} = 135 \pm 36$ mas yr^{-1} for CWISE J215859.63−085441.9 and $\mu_{tot} = 53 \pm 5$ mas yr^{-1} for CWISE J235713.17-630827.3, as measured by CatWISE. Finder charts of the two M dwarfs (Figure 5) show the slow proper motion. Using the CatWISE2020 proper motion data and the distance estimate we

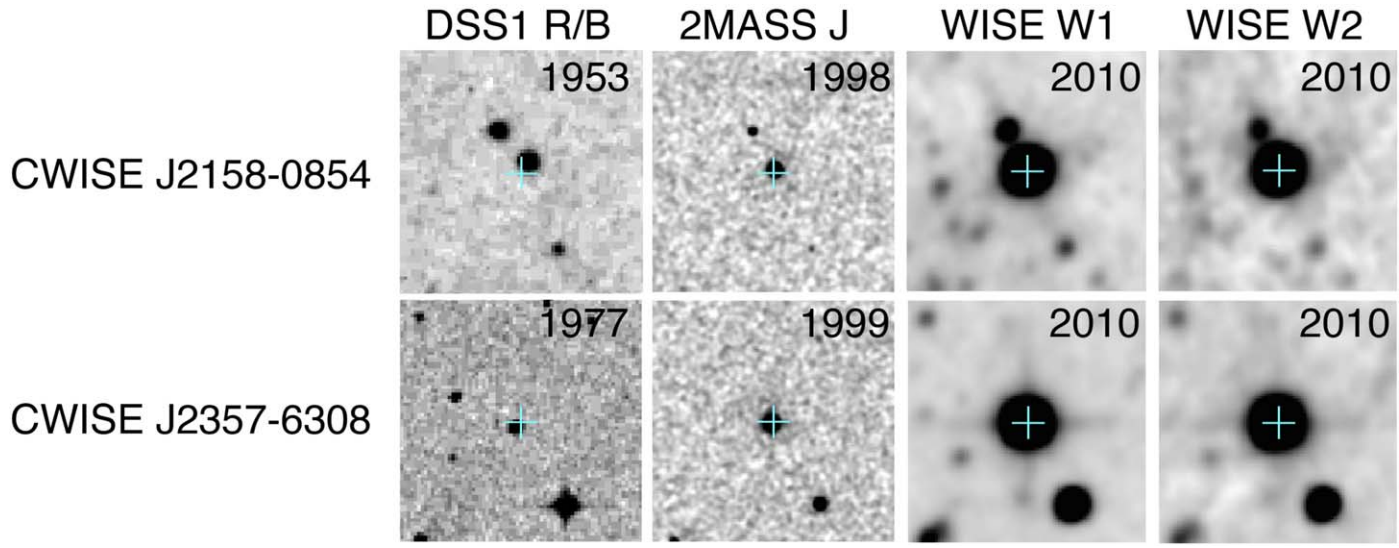

Figure 5. Finder charts for CWISE J2158−0854 and CWISE J2357−6308. The finder chart shows a >30 yr baseline of time. DSS2 R, 2MASS J, WISE W1, and WISE W2 images are shown. The objects have small but clear proper motions. Each cutout is 2′ on a side, with north up and east to the left.

calculated above, we estimated the tangential velocity of CWISE J215859.63−085441.9 to be 6.1 km s^{-1}. Again, assuming an equal-magnitude pair, the tangential velocity estimate for CWISE J235713.17-630827.3 is 4.5 km s^{-1}.

The two M dwarfs were initially flagged as outliers when we plotted them using their reported VHS magnitudes. However, these magnitudes differ markedly from the 2MASS magnitudes. For example, CWISE J215859.63−085441.9 has VHS magnitudes of $J_{MKO} = 11.868 \pm 0.001$ and $Ks_{VHS} = 11.205 \pm 0.001$ mag, whereas it has 2MASS magnitudes of $J_{2MASS} = 11.215 \pm 0.026$ and $Ks_{2MASS} = 10.470 \pm 0.025$ mag. The differences between the VHS and 2MASS magnitudes are $\Delta J = 0.653$ and $\Delta Ks = 0.735$ mag. This difference is larger than what we can attribute to the difference in filter sets. We believe the 2MASS data are credible and the VHS data problematic for the following reasons: (1) We know that 2MASS magnitudes are valid between $-4 < Ks < 16$ mag,[16] and our source falls within this range. (2) VHS data has a bright limit (11.5–12 mag) where sources saturated and where the reported magnitudes cannot be properly measured (González-Fernández et al. 2018). Our objects are brighter than this limit. Thus, the difference in magnitudes is caused by saturation in the VHS data. Using the 2MASS magnitudes, the colors of both objects are consistent with M dwarfs, and they are no longer color-color outliers.

4.2. CWISE J123041.80+380140.9

CWISE J123041.80+380140.9 is a high proper motion object ($\mu_{tot} = 764 \pm 115$ mas yr^{-1}). We used the W1 − W2 color of 0.879 ± 0.117 mag and the color versus spectral type relation found in Table 13 of Kirkpatrick et al. (2021) to estimate a spectral type of ∼T2. Based on Figure 3, the $J - W2$ versus W1 − W2 location is consistent with an early-T dwarf.

The finder chart (Figure 6) of our object illustrates its faintness. The object is not detected by 2MASS, but it is faintly detected in UHS and more clearly detected in WISE.

From the same paper and table, we used the absolute magnitude versus color relation to derive an absolute W2 value of 12.3 mag, which implies a distance of ∼74 pc using the apparent W2 magnitude. Using the CatWISE2020 proper motion and distance estimate, we calculate a tangential velocity of ∼234 km s^{-1}. We theorize that the high velocity of this object is likely caused by dynamical heating, which implies an old age. Furthermore, old age often implies low metallicity. Oddly, however, the object falls on the normal T dwarf track, so future spectroscopic observations are needed to reveal its nature.

4.3. CWISE J184842.02-875747.9

CWISE J184842.02-875747.9[17] falls along the L dwarf track, as seen in Figures 2 and 3. A finder chart is shown in Figure 6. We used the W1 − W2 color of 0.659 ± 0.026 mag and the color versus spectral type relation found in Table 13 of Kirkpatrick et al. (2021) to estimate a spectral classification of ∼L7.5. From the same paper and table, we used the absolute magnitude versus color relation to derive an absolute W2 value of 12.2 mag, which implies a distance of ∼29 pc, using the apparent W2 magnitude. A color of $J - W2 = 4.23 \pm 0.13$ mag is surprisingly red for an L dwarf. The only L dwarfs that are this red in Figure 14 of Kirkpatrick et al. (2021) are young objects. In addition, the only L dwarfs that rival this J − W2 color in Figure 8 of Faherty et al. (2016) are young objects. Using the $W2_{YNG}$ versus spectral type relation found in Table 19 of Faherty et al. (2016), we derived an absolute W2 value of 10.8 mag, which implies a distance of ∼54 pc using the apparent magnitude. If the object is determined to be young, the true distance should be closer to this value than the 29 pc distance value estimated above. Using the CatWISE2020 proper motion ($\mu_{tot} = 158 \pm 15$ mas yr^{-1}) and the distance estimate if the object is young, we calculate a tangential velocity of ∼35 km s^{-1}, which would not run counter to the young classification. We therefore propose that this is likely a

[16] See: https://irsa.ipac.caltech.edu/data/2MASS/docs/releases/allsky/doc/sec2_2b.html.

[17] CWISE J184901.34-875753.4 lies 11.″2 to the southeast. Although the CatWISE2020 catalog measures no significant proper proper motion, it appears to be moving in the WiseView blink. However, this proper motion is not aligned with CWISE J184842.02-875747.9.

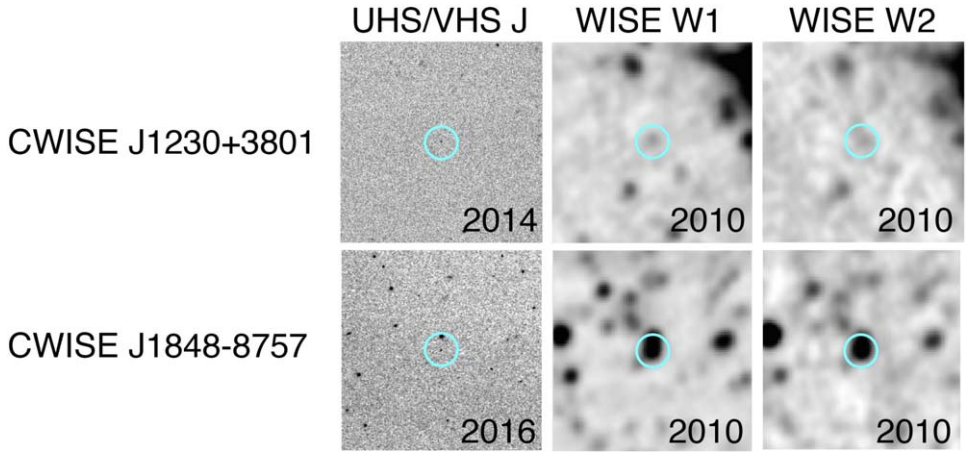

Figure 6. Finder charts for CWISE J1230+3801 and CWISE J1848−8757. The finder charts illustrate the faintness of the objects. The UHS J, WISE W1, and WISE W2 images are shown for CWISE J1230+3801. The VHS J, WISE W1, and WISE W2 images are shown for CWISE J1848-8757. Each cutout is 2′ on a side, with north up and east to the left.

candidate young L dwarf. However, using the CatWISE2020 proper motion data, we find no clear membership in any young nearby moving group from Banyan Σ (Gagné et al. 2018), and it is determined to be a field object with 99% probability. Future spectroscopic observations of CWISE J184842.02-875747.9 would help determine whether it is young via low-gravity spectral features (Allers & Liu 2013).

4.4. Additional Discovered Objects

The remaining 16 objects are discussed further below.

1. CWISE J044109.35+254854.4 falls in an unusual spot in Figures 2 and 3 at colors of $J - W2 > 5.8$ mag, $J\text{-}K > 3.7$ mag, and $W1 - W2 = 1.031 \pm 0.016$ mag. Objects that lie in this portion of the diagram are either extremely red L dwarfs or reddened objects (cf. Figures 7 and 8 of Kirkpatrick et al. 2016). The coordinates place the object in a region of nebulosity toward the Taurus molecular cloud. Thus, we surmise that the object is behind the cloud and is being reddened by it. CWISE J044109.35+254854.4 has a motion significance of 21 σ ($\mu_{\rm tot} = 160 \pm 7.5$ mas yr^{-1}). In addition, this source appears point-like and exhibits clear motion between the 1998-epoch 2MASS Ks image and the 2010-epoch AllWISE W1/W2 images, further confirming the proper motion measured by CatWISE2020. A spectrum of this object is needed to measure a spectral type and the amount of extinction, estimate a distance, and confirm whether the distance is sufficient to place the object behind the cloud.
2. CWISE J030009.79+413051.2 is likely a late-T dwarf. This object was not detected by 2MASS and was only found in UHS and WISE. We used the $J - W2$ color of 3.22 ± 0.18 mag and the color versus spectral type relation found in Table 13 of Kirkpatrick et al. (2021) to estimate a spectral classification of T8. As shown in Figure 3, this object falls along the normal late-T dwarf track. From the same paper and table, we used the absolute magnitude versus color relation to derive an absolute W2 value of 13.0 mag, which implies a distance of ∼40 pc using the apparent W2 magnitude.
3. CWISE J040052.80-511142.5 and CWISE J184048.17+410727.4 have a motion significance of only 1.3σ and 1.0 σ, respectively, in CatWISE2020 (see Table 1), giving us little confidence that the objects are nearby. However, when querying the NOIRLab Source Catalog, we find that CWISE J040052.80-511142.5 has a motion significance of 4.3 σ ($\mu_{\rm tot} = 98 \pm 23$ mas yr^{-1}). The location of CWISE J184048.17+410727.4 is unfortunately not covered by the NOIRLab Source Catalog. However, Figure 7 shows that the overall colors from the optical to the mid-infrared of both objects correspond to those of T dwarfs. Using the methodology above, we estimated spectral types of T7.5 for CWISE J040052.80-511142.5 and T8.5 for CWISE J184048.17+410727.4, which correspond to 31 and 27 pc, respectively. To confirm these classifications, spectra are needed.
4. CWISE J103716.55-750257.7 and CWISE J125924.86-552531.8 are two likely L dwarfs. We used the $W1 - W2$ color of 0.23 ± 0.07 mag and the color versus spectral type relation found in Table 13 of Kirkpatrick et al. (2021) to estimate a spectral classification of L2.5 for CWISE J103716.55-750257.7. From the same paper and table, we used the absolute magnitude versus color relation to derive an absolute W2 value of 12.0 mag, which implies a distance of ∼37 pc using the apparent W2 magnitude. Using the methodology above, CWISE J125924.86-552531.8 has a spectral type of L4 and a distance of ∼36 pc.
5. CWISE J141545.74-330545.0 and CWISE J210159.84-783846.8 have measurements in all three colors found in Figures 2 and 3. Their locations in these figures when compared to Figure 7 and 8 of Kirkpatrick et al. (2016) are consistent with L subdwarfs or early-T dwarfs. Spectra are needed for both objects to determine their nature and to estimate distances.
6. CWISE J120657.58-311221.1 also has measurements in all three colors found in Figures 2 and 3. Its location is consistent with an M subdwarf. Using its Gaia EDR3 parallax, we calculate a distance of ∼156 parsecs. Then, using the Gaia EDR3 proper motion data (($\mu_{\rm tot} = 534 \pm 23$ mas yr^{-1}) and distance, we calculate a very high tangential velocity of ∼394 km s^{-1}.

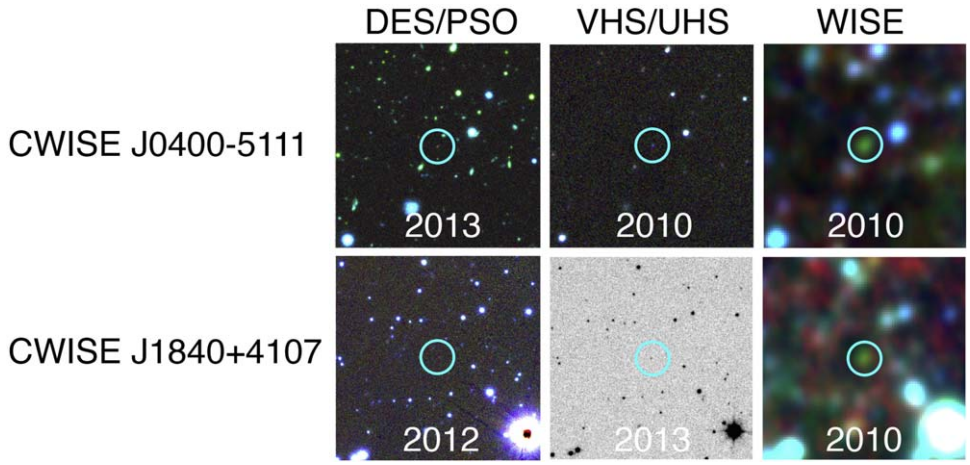

Figure 7. Finder charts for CWISE J0400−5111 and CWISE J1840+4107. For CWISE J0400-5111 these are three-color images made from DES g, i, and y, VHS J, H, and Ks, and WISE W1, W2, and W3. For WISE J1840+4107, the images are PSO g, i, and y, UHS J, and WISE W1, W2, and W3. (Only one band was available for UHS.) For CWISE J0400-5111, the red color in the optical (DES), the blue color in the near-infrared (VHS), and the green color in the mid-infrared (WISE) parallel the spectral energy distribution of a T dwarf. CWISE J1840+4107 has less information than CWISE J0400−5111, but is faint in the optical, detected at J, and brighter and green in the WISE bands, again characteristic of a T dwarf.

7. All of the following objects are outliers, but not for astrophysical reasons. CWISE J144053.88-121712.3 lies near another object, leading to contaminated photometry. CWISE J052703.28-113056.7 and CWISE J015330.24-520046.6 are close comoving doubles. WISE has combined photometry from both sources, while VHS reports photometry from both, which leads to inaccurate J − W2 colors.

5. Conclusion

We have presented 16 new dwarfs identified through supervised learning methods. Specifically, we highlight four interesting objects: two nearby M dwarfs (CWISE J215859.63−085441.9, CWISE J235713.17−630827.3), a high proper motion early-T dwarf (CWISE J123041.80+380140.9), and one likely young L dwarf (CWISE J184842.02-875747.9).

Spectroscopy will help to reveal the nature of these objects. For the M dwarfs, this will be used to obtain more definitive spectral classifications and distance estimates. We also await future Gaia data to confirm the binary hypothesis. For the high proper motion T dwarf, a spectrum would confirm the spectral type and metallicity. Finally, a spectrum of the suspected young L dwarf would be used to search for features of low gravity, which is a direct indicator of youth.

There are a few limitations to our search method described in Section 2. First, because we are searching for nearby objects through their significant proper motions, we are not sensitive to nearby objects with small, insignificant proper motions. Second, some of our objects are not detected by 2MASS. Of these, some lack deeper UHS or VHS data, while others are undetected in their UHS or VHS images. Without detections in these data, we are not able to use our color–color diagrams to select interesting objects. Additional analysis must also be performed on the objects in the candidate list with UHS and VHS imaging that lack a detection in their respective images. This means that UHS and VHS failed to detect the objects at the sensitivities of those surveys. This is relevant because the elusive Y dwarfs (Kirkpatrick et al. 2012) may be tucked away in this exclusive list of objects.

This paper represents just one way to search through the CatWISE2020 data. The entire CatWISE2020 and Backyard Worlds team is employing a myriad of methods for analyzing WISE data, and this will culminate in new insights about the luminosity and mass functions (J. D. Kirkpatrick et al. 2022, in preparation). Our approach is just one machine learning method applied to WISE catalog data. Other machine learning methods have used different training sets to explore new areas of parameter space or they have used WISE imaging data (D. Caselden 2022, in preparation). There are other approaches that do not use machine learning, such as using catalog selection (Meisner et al. 2020) directly from IRSA or human vetting of motion candidates (Kuchner et al. 2017). All of these methods will help researchers to fully explore the almost 1.8 billion sources in the CatWISE2020 catalog and the epochal coadds from the unWISE collection, and they will undoubtedly aid in uncovering even more interesting objects.

Our research illustrates that, despite our best efforts over the last decade, there are still discoveries near the Sun to be made. In addition, our census of the faintest stellar and substellar objects is still incomplete. To complete the census, astronomers (and the public!) are encouraged to continue exploring CatWISE2020 and exploit its capabilities.

CatWISE is funded by NASA under Proposal No. 16-ADAP16-0077 issued through the Astrophysics Data Analysis Program, and uses data from the NASA-funded WISE and NEOWISE projects. This research has made use of the NASA/IPAC Infrared Science Archive, which is funded by the National Aeronautics and Space Administration and operated by the California Institute of Technology. The Backyard Worlds: Planet 9 team would like to thank the many Zooniverse volunteers who have participated in this project, from providing feedback during the beta review stage to classifying flipbooks to contributing to the discussions on TALK. We would also like to thank the Zooniverse web development team for their work creating and maintaining the Zooniverse platform and the Project Builder tools. F.M. acknowledges support from grant 80NSSC20K0452 under the NASA Astrophysics Data Analysis Program. This research was supported by NASA grant 2017-ADAP17-0067. This

material is based upon work supported by the National Science Foundation under grant No. 2007068, 2009136, and 2009177. This research has made use of the SIMBAD database, operated at CDS, Strasbourg, France. This publication makes use of data products from the Two Micron All-Sky Survey, which is a joint project of the University of Massachusetts and the Infrared Processing and Analysis Center/California Institute of Technology, funded by the National Aeronautics and Space Administration and the National Science Foundation. This publication makes use of data products from the Near-Earth Object Wide-field Infrared Survey Explorer (NEOWISE), which is a joint project of the Jet Propulsion Laboratory/California Institute of Technology and the University of Arizona. NEOWISE is funded by the National Aeronautics and Space Administration. Our research used data from the UHS collaboration and the VISTA Hemisphere Survey (VHS). We wish to thank the Student Astrophysics Society[18] for providing the resources that enabled the pairing of highschool and undergraduate students with practicing astronomers and advanced citizen scientists. We thank the anonymous referee for insightful suggestions that helped improve the manuscript.

Facilities: WISE/NEOWISE, 2MASS, UKIRT, VISTA .

Software: Astropy: Astropy Collaboration et al. (2013), Banyan Σ: Gagné et al. (2018), TOPCAT: Taylor (2005) XGBoost: Chen & Guestrin (2016), WiseView: Caselden et al. (2018).

ORCID iDs

Tarun Kota https://orcid.org/0000-0001-8764-7648
J. Davy Kirkpatrick https://orcid.org/0000-0003-4269-260X
Dan Caselden https://orcid.org/0000-0001-7896-5791
Federico Marocco https://orcid.org/0000-0001-7519-1700
Adam C. Schneider https://orcid.org/0000-0002-6294-5937
Jonathan Gagné https://orcid.org/0000-0002-2592-9612
Jacqueline K. Faherty https://orcid.org/0000-0001-6251-0573
Aaron M. Meisner https://orcid.org/0000-0002-1125-7384
Marc J. Kuchner https://orcid.org/0000-0002-2387-5489
Sarah Casewell https://orcid.org/0000-0003-2478-0120
Kanishk Kacholia https://orcid.org/0000-0001-9878-0436
Tom Bickle https://orcid.org/0000-0003-2235-761X
Guillaume Colin https://orcid.org/0000-0002-7630-1243
Leslie K. Hamlet https://orcid.org/0000-0002-7389-2092
Jörg Schümann https://orcid.org/0000-0002-7587-7195

References

Abbott, T. M. C., Abdalla, F. B., Allam, S., et al. 2018, ApJS, 239, 18
Allers, K. N., & Liu, M. C. 2013, ApJ, 772, 79
Astropy Collaboration, Robitaille, T. P., Tollerud, E. J., et al. 2013, A&A, 558, A33
Caselden, D., Westin, P., Meisner, A., et al. 2018, Astrophysics Source Code Library, ascl:1806.004
Chen, T., & Guestrin, C. 2016, arXiv:1603.02754
Connors, M., Wiegert, P., & Veillet, C. 2011, Natur, 475, 481
Chambers, K. C., Magnier, E. A., Metcalfe, N., et al. 2016, arXiv:1612.05560
Cutri, R. M., Wright, E. L., Conrow, T., et al. 2013, Explanatory Supplement to the AllWISE Data Release Products
Dye, S., Lawrence, A., Read, M. A., et al. 2018, MNRAS, 473, 5113
Eisenhardt, P. R. M., Marocco, F., Fowler, J. W., et al. 2020, ApJS, 247, 69
Faherty, J. K., Riedel, A. R., Cruz, K. L., et al. 2016, ApJS, 225, 10
Gagné, J., Mamajek, E. E., Malo, L., et al. 2018, ApJ, 856, 23
Gaia Collaboration, Prusti, T., de Bruijne, J. H. J., et al. 2016, A&A, 595, A1
Gillon, M., Triaud, A. H. M. J., Demory, B.-O., et al. 2017, Natur, 542, 456
González-Fernández, C., Hodgkin, S. T., Irwin, M. J., et al. 2018, MNRAS, 474, 5459
Kiman, R., Schmidt, S. J., Angus, R., et al. 2019, AJ, 157, 231
Kirkpatrick, J. D., Gelino, C. R., Cushing, M. C., et al. 2012, ApJ, 753, 156
Kirkpatrick, J. D., Schneider, A., Fajardo-Acosta, S., et al. 2014, ApJ, 783, 122
Kirkpatrick, J. D., Kellogg, K., Schneider, A. C., et al. 2016, ApJS, 224, 36
Kirkpatrick, J. D., Martin, E. C., Smart, R. L., et al. 2019, ApJS, 240, 19
Kirkpatrick, J. D., Gelino, C. R., Faherty, J. K., et al. 2021, ApJS, 253, 7
Kuchner, M. J., Faherty, J. K., Schneider, A. C., et al. 2017, ApJL, 841, L19
Luhman, K. L. 2013, ApJL, 767, L1
Luhman, K. L., & Esplin, T. L. 2014, ApJ, 796, 6
Mainzer, A., Bauer, J., Grav, T., et al. 2011, ApJ, 731, 53
Mainzer, A., Bauer, J., Grav, T., et al. 2014, ApJ, 784, 110
Marocco, F., Caselden, D., Meisner, A. M., et al. 2019, ApJ, 881, 17
Marocco, F., Eisenhardt, P. R. M., Fowler, J. W., et al. 2021, ApJS, 253, 8
McMahon, R. G., Banerji, M., Gonzalez, E., et al. 2013, Msngr, 154, 35
Meisner, A. M., Caselden, D., Kirkpatrick, J. D., et al. 2020, ApJ, 889, 74
Meisner, A. M., Schneider, A. C., Burgasser, A. J., et al. 2021, arXiv:2106.01387
Pecaut, M. J., & Mamajek, E. E. 2013, ApJS, 208, 9
Ricker, G. R., Winn, J. N., Vanderspek, R., et al. 2015, JATIS, 1, 014003
Rothermich, A., Faherty, J., Bardalez Gagliuffi, D., et al. 2021, BAAS, 53, 2021n1i414p03
Schlafly, E. F., Meisner, A. M., & Green, G. M. 2019, ApJS, 240, 30
Skrutskie, M. F., Cutri, R. M., Stiening, R., et al. 2006, AJ, 131, 1163
Taylor, M. B. 2005, in ASP Conf. Ser. 347, Astronomical Data Analysis Software and Systems XIV, ed. P. Shopbell, M. Britton, & R. Ebert (San Francisco, CA: ASP), 29
Tsai, C.-W., Eisenhardt, P. R. M., Wu, J., et al. 2015, ApJ, 805, 90
Wenger, M., Ochsenbein, F., Egret, D., et al. 2000, A&AS, 143, 9
Wright, E. L., Eisenhardt, P. R. M., Mainzer, A. K., et al. 2010, AJ, 140, 1868
Zechmeister, M., Kürster, M., & Endl, M. 2009, A&A, 505, 859

[18] https://www.studentastrophysicssociety.com